






Article

# Hyperspectral Image Dimensionality Reduction via Maximum Information Tensor Bands Selection for Classification with Convolutional Neural Networks

Josué López <sup>1,\*</sup> , Deni Torres <sup>1</sup> , Clement Atzberger <sup>2</sup> , Andrea González <sup>1</sup>  and Israel Yañez <sup>3</sup> 

<sup>1</sup> Center for Research and Advanced Studies of the National Polytechnic Institute, Telecommunications Group, Av del Bosque 1145, Zapopan 45017, Mexico; deni.torres@cinvestav.mx; andrea.gonzalez@cinvestav.mx

<sup>2</sup> University of Natural Resources and Life Science, Institute of Geomatics, Peter Jordan 82, Vienna 1180, Austria; clement.atzberger@boku.ac.at

<sup>3</sup> Polytechnic University Juventino Rosas, Networks and Telecommunications Ingengering Department, Miguel Hidalgo 102, Comunidad de Valencia 38253 Juventino Rosas, Guanajuato, Mexico; jyanezptc@upjr.edu.mx

\* Correspondence: josue.lopez@cinvestav.mx

Version January 7, 2021 submitted to Remote Sens.

**Abstract:** Tensor-based decomposition for compression of high dimensionality datasets have been widely used in recent years in several research areas, including Multi- and Hyperspectral Images (MSI and HSI) processing. On the other hand, Convolutional Neural Networks (CNNs) are specialized kind of Artificial Neural Networks (ANNs) for processing data that has a known grid-like topology and belongs to the set of natural numbers, such as image data. Compression of the input data of a CNN induce poor performance in tasks, such as classification and semantic segmentation. In this paper, Tucker-based models are employed to reduce the dimensionality in the spectral domain of MSIs and HSIs to reduce the complexity of a pixel-wise classification CNN, while preserving high performance. We propose a framework, based on information theory, that performs a characterization of a spectral dataset, by computing the entropy and the probability distribution function of the spectral bands, as well as a quantification of orthogonality and divergence of the compressed data, to define the dimensionality of the CNN input tensor. Besides, we propose an alternative Tucker approximation with non-negativity and integer constraints called Integer Approximation Non-negative Tucker Decomposition (IANTD). Experimental results demonstrate...

**Keywords:** entropy; hyperspectral imagery; tensor decomposition

## 1. Introduction

Dimensionality reduction of dataset for machine learning algorithms has been one of the most active research areas in recent years []. The introduction of tensor-based models for these kind of tasks inspired a change in several areas, such as image processing [].

Particularly, Remote Sensing (RS) image processing is focused on detecting and monitoring physical features about areas of interest, by analyzing the reflectance of materials over the earth surface. Some remote sensors use filters to separate the reflectance of an object in different wavelength ranges []. These sensors generate the well-known Multi- (MSI) and Hyper-spectral Images (HSI), which lead to high performance in image processing tasks such as detection, classification and segmentation []. Besides, in the last few years the use of spectral data has grown exponentially in other fields as medical analysis [], biomedical [], and, in RS fields as agriculture [], natural disaster prevention [], security affairs [], among others [].

In the last decade, many supervised classification and segmentation algorithms were developed, with the aim of taking advantage of the spatial and spectral data features provided by RS MSI and HSI. Support Vector Machines (SVM) [], k-Nearest Neighbors (k-NN) [] and Convolutional Neural Networks (CNN) [] are examples of the aforementioned. Spectral image processing in artificial intelligence algorithms increase drastically the execution time [], which forces to have robust computer equipment to achieve time competitive results.

Withn the aim of reducing high-dimensionality of spectral images, some authors developed dimensionality reduction strategies, by selecting the most salient spectral bands [], and by maximum information and minimum redundancy criteria, based on entropy and mutual information metrics []. These approaches have the advantage of preserving the original domain of MSIs and HSIs. Other works opted for matrix factorization methods, such as Principal Component Analysis (PCA) [] and Singular Values Decomposition (SVD) []. Recently, tensor-based factorization algorithms have proven to be advantageous over those based on matrices []. Nevertheless, changing the input data domain of a machine learning model could lead to a drop in its performance [].

In this work, we propose an innovative spectral imagery dimensionality reduction method from the perspective of maximum information analysis, in which the spectral signatures are carried to a new domain through tensor decompositions. We also propose an Integer Approximation Non-negative Tucker Decomposition (IANTD) with non-negativity and integer constraints, alternative to the basic Tucker Decomposition (TKD) and the Non-negative Tucker Decomposition (NTD). This has the aim of achieving high performance in pixel-wise classification CNNs with low dimensionality input data. The proposed method can be seen as a three stages process. In the first stage, the original spectral image is factorized, through a Tucker-based model, transforming the spectral signatures from pixel reflectance domain into *tensor signatures*. In the second stage, a band selection is developed based on an entropy criterion to reduce data dimensionality. By last, the compressed tensor is used as input to a pixel-wise classification CNN meant to keep high classification performance. The experimental results on public available dataset show that the proposed framework decrease efficiently the computational complexity of the classification CNN with a 10x speedup in testing execution time. Besides, this approach achieves competitive performance,  $\pm 2.1\%$  Pixel Accuracy (PA), with lower data dimensionality compared with previous works.

### 1.1. Previous works

In recent years, several researchers have developed methods to reduce computational complexity of machine learning algorithms [], specially, for HSI classification with Deep Learning (DL) Artificial Neural Networks (ANNs) []. The crucial factor addressed in this work is, to achieve MSI and HSI compression reducing the high computational complexity, without decreasing classification performance in CNNs.

The first methods used for HSI compression was band selection. Li et al. in [23] proposed a band selection method from the perspective of spectral shape similarity analysis. Saliency of spectral bands was another popular approach. Wang Q. et al. [22] proposed to eliminate the drawbacks of traditional salient band selection methods by manifold ranking. More recently, P. Wang et al [] introduced image fusion for feature reduction with joint sparsity model. Besides, other researchers focused their efforts in compressing HSI spectral bands from an information theory point of view. Arecent example is Tschannerl et al. [], who proposed a band selection algorithm following the Maximum-Information-Minimum-Redundancy (MIMR) criterion that maximises the information carried by individual features of a subset and minimizes redundant information between them, as done in [].

Later, matrix decomposition methods were used, such as PCA in [? ], and even non-negative matrix decomposition methods [? ]. Nevertheless, matrix-based methods are limited to data representations in 2-dimensional spaces. Spectral imagery have data structures as 3rd-order arrays. This 2-way view produces considerable loss in information, and in turn, in further processing

**Table 1.** Related work to compression and classification of spectral imagery.

Author & year	Data	Decomposition	Compression	Classifier
Li, S. et al. [23] (2014)	HSI	-	Band selection	SVM
Zhang, L. et al. [24] (2015)	HSI	TKD	Spatial-Spectral	-
Wan, Q. et al. [22] (2016)	HSI	-	Band selection	SVM/kNN/CART
Tong L. et al. [] (2017)	HSI	NMF	Unmixing	-
Chien, J. et al. [] (2017)	RGB	TFNN	Spatial-Spectral	TFNN
Dewa, M. et al. [] (2018)	HSI	PCA	Spectral	PCA
Xu, Y. et al. [] (2018)	HSI	-	-	CNN
Li, J. et al. [28] (2019)	MSI	NTD-CNN	Spatial-spectral	-
An, J. et al. [27] (2019)	HSI	T-MLRD	Spatial-spectral	SVM/1NN
An, J. et al. [29] (2019)	HSI	TDA	Spatial-spectral	SVM/1NN
Sayeh, M. et al [] (2019)	HSI	NTD	Spatial-Spectral	3D-CNN
Lopez, J. et al. [] (2020)	MSI	TKD	Spectral	FCN
Sayeh, M. [] (2020)	HSI	BG-NTD	Spatial-Spectral	MLR
<b>Our framework</b>	<b>MSI/HSI</b>	<b>IANTD/NTD</b>	<b>Spectral</b>	<b>CNN</b>

performance. In 2015 Zhang et al. [24] were pioneers in experimenting with multilinear algebra-based decompositions on hyperspectral images.

On the other hand, instead of HSI, MSIs was a good alternative due to the small number of spectral bands, which also produce competitive classification performance [11], [18], [21] and [? ]. However, the need to increase performance forced researchers to use data with higher number of spectral bands, which ease classification of materials hard to differentiate [26], [27], [29], [? ] and [? ].

Recently, a work close to our research was published. Sayeh [? ] proposed a framework where discriminative features are extracted applying Non-negative Tensor Decomposition (NTD) technique to the image tensor. The factorized components indicate the spectral signatures and 2D abundance maps of the constituent materials. Different to our framework, they compress HSI in the spatial and spectral domain, while our approach preserve the architecture of the image by compressing only the spectral domain and with non-negativity constraints in the core tensor of the TKD. In addition, we introduce information metrics to reinforce the rank estimation method proposed in [] and we propose an integer approximation to take advantages of the kindness of CNNs. Table 1 summarizes some related papers, which deal with the compression-classification issue.

## 1.2. Motivation

Dimensionality reduction in HSI processing is still a challenging issue. The recent rise of DL-ANN in the image processing area has led researchers to find ways to preserve the spatial-spectral information of HSI in lower dimensionality than the raw data. Several methods have been proposed in the last five years. However, band selection, matrix factorization, as well as tensor-based methods proposed previously perform dimensionality reductions that, to obtain competitive performance, still require more than twenty percent of the data, which still maintain high computational complexity.

In this work, we address the HSIs dimensionality reduction issue by applying a non-negative Tucker-based decomposition to take original data into a new tensor domain, where the spatial-spectral features are contained in a lower dimensionality tensor than the raw data. With the aim of keeping high classification performance with the compressed data, this work presents an information quantification strategy, to avoid high information loss, while reducing computational complexity of pixel-wise classification CNNs. This work has three particular motivations: 1) to reduce the computational complexity of CNNs, 2) to avoid overfitting, and 3) to keep high classification performance in lower execution time.

### 1.3. Contribution

Unlike previous works, we address the problem of HSI dimensionality reduction by a tensor factorization and entropy approach. The main contributions of this work can be summarized by the following two points:

1. We propose a HSI band selection strategy combined with a tensor decomposition approach, where the most of the information is leaded to a lower dimensionality non-negative tensor, obtaining a high level representation of the raw data.
2. Besides, we propose a novel integer non-negative Tucker-based approximation, called (IANTD), where the decomposition is restricted to output an integer non-negative core tensor with the same dimensionality of the raw data, regarded to own high entropy levels in the front new tensor bands.
3. This work also presents a Linear Mixing Model analysis to relate spectral signatures from the raw data with the tensor signatures formed in the new tensor bands generated by Tucker-1 based decompositions.

The remainder of this work is organized as follows. Section 2 introduces tensor algebra notation and basic concepts to familiarize the reader with the symbology used in this paper. Section 3 describes the problem statement and the framework proposed in this work. Experimental results are presented in Section 4. Finally, Sections 5 and 6 present the discussions, comparisons and conclusions based on the experimental results obtained in the cases studied.

## 2. Preliminaries

As defined formally in [], an  $N$ th-order tensor is an element of the tensor product of  $N$  vector spaces, each of which has its own coordinate system. A tensor can be seen as a multidimensional array. The order of a tensor is the number of dimensions, also known as modes, i.e., an  $N$ -order tensor  $\mathcal{X} \in \mathbb{R}^{I_1 \times I_2 \times \dots \times I_N}$  is an  $N$ -dimensional array, which elements  $x_{i_1, i_2, \dots, i_n}$  are indexed by  $i_n \in 1, 2, \dots, I_n$  for  $1 \leq n \leq N$ . Throughout this paper, the mathematical notation used by Kolda et al. [17] has been adopted. Table 2 summarize this notation.

### 2.1. Tensor decompositions (TDs)

As an extension of the SVD [], two main specific tensor decompositions can be considered, Tucker Decomposition (TKD) [] and CANDECOMP/PARAFAC (CP) []. There are many other tensor decompositions, INDSCAL, PARAFAC2, CANDELINC, DEDICOM, PARATUCK2, among others [17]. Furthermore, there are also nonnegative variants of all of the above. With the aim of preserving particular characteristics of hyperspectral images for pixel-wise classification, this study is limited to use decompositions based on the Tucker model.

#### 2.1.1. Tucker Decomposition (TKD)

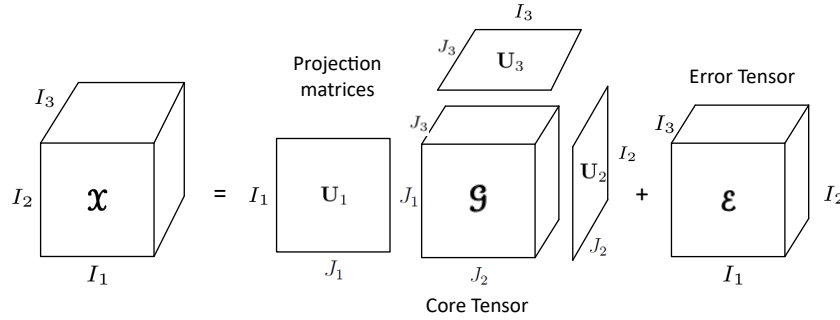
For the particular case of third-order tensors, the TKD [17] can be formally formulated as follows [?]. Given a third-order tensor  $\mathcal{X} \in \mathbb{R}^{I_1 \times I_2 \times I_3}$  and three positive indices  $J_1, J_2$  and  $J_3$ , find a core tensor  $\mathcal{G} \in \mathbb{R}^{J_1 \times J_2 \times J_3}$  and three component matrices called factor matrices  $\mathbf{U}^{(1)} \in \mathbb{R}^{I_1 \times J_1}$ ,  $\mathbf{U}^{(2)} \in \mathbb{R}^{I_2 \times J_2}$  and  $\mathbf{U}^{(3)} \in \mathbb{R}^{I_3 \times J_3}$  which perform the following approximate decomposition:

$$\mathcal{X} = \mathcal{G} \times_1 \mathbf{U}^{(1)} \times_2 \mathbf{U}^{(2)} \times_3 \mathbf{U}^{(3)} + \mathcal{E} \quad (1)$$

where  $\mathcal{E}$  denotes the approximation error. The core tensor  $\mathcal{G}$  preserves the level of interaction for each factor or projection matrix  $\mathbf{U}^{(n)}$ . The factor matrices are commonly considered orthogonal, but in Tucker models with non-negativity constraints, that is not necessarily imposed [?]. These matrices can be seen as the principal components in each mode [17] (see Figure 1).  $J_n$  represents the number

**Table 2.** Tensor algebra notation summary

$\mathcal{A}, \mathbf{A}, \mathbf{a}, a$	Tensor, matrix, vector and scalar respectively
$\mathcal{A} \in \mathbb{R}^{I_1 \times \dots \times I_N}$	$N$ -order tensor of size $I_1 \times \dots \times I_N$ .
$a_{i_1 \dots i_N}$	An element of a tensor
$\mathbf{a}_{:i_2 i_3}, \mathbf{a}_{i_1 : i_3},$ and $\mathbf{a}_{i_1 i_2 :}$	Column, row and tube fibers of the third order tensor $\mathcal{A}$
$\mathbf{A}_{i_1 ::}, \mathbf{A}_{:i_2 :}, \mathbf{A}_{::i_3}$	Horizontal, lateral and frontal slices of the third order tensor $\mathcal{A}$
$\mathbf{A}^{(n)}, \mathbf{a}^{(n)}$	A matrix/vector element from a sequence of matrices/vectors
$\mathbf{A}_{(n)}$	Mode- $n$ matricization of a tensor. $\mathbf{A}_{(n)} \in \mathbb{R}^{I_n \times \prod_{m \neq n} I_m}$
$\mathbf{a}^{(1)} \circ \dots \circ \mathbf{a}^{(N)}$	Outer product of $N$ vectors
$\langle \mathcal{A}, \mathcal{B} \rangle$	Inner product of two tensors
$\mathcal{B} = \mathcal{A} \times_n \mathbf{U}$	$n$ -mode product of tensor $\mathcal{A} \in \mathbb{R}^{I_1 \times \dots \times I_N}$ by a matrix $\mathbf{U} \in \mathbb{R}^{J \times I_n}$ along axis $n$
$\text{rank}_n(\mathcal{X})$	column rank of $\mathbf{X}_{(n)}$ . If $R_n \equiv \text{rank}_n(\mathcal{X})$ , then $\mathcal{X}$ has a rank $-(R_1, \dots, R_N)$ tensor

**Figure 1.** Tucker decomposition for a third-order tensor.

of components in the decomposition, i.e., the rank  $-(R_1, R_2, R_3)$ . The core tensor is computed by the multilinear projection

$$\mathcal{G} = \mathcal{X} \times_1 \mathbf{U}^{(1)T} \times_2 \mathbf{U}^{(2)T} \times_3 \mathbf{U}^{(3)T} \quad (2)$$

where  $\mathbf{U}^{(n)T}$  denotes the transpose matrix of  $\mathbf{U}^{(n)}$  for  $n = 1, \dots, N$ . Hence, the approximation  $\hat{\mathcal{X}}$  of the tensor decomposition is given by

$$\hat{\mathcal{X}} = \mathcal{G} \times_1 \mathbf{U}^{(1)} \times_2 \mathbf{U}^{(2)} \times_3 \mathbf{U}^{(3)}. \quad (3)$$

Hence, the reconstruction error  $\zeta$  can be computed as

$$\zeta(\hat{\mathcal{X}}) = \|\mathcal{X} - \hat{\mathcal{X}}\|_F^2 \quad (4)$$

and  $\|\cdot\|_F$  represents the Frobenius norm. To compute the  $\text{rank}_n(\mathcal{X})$  approximation of a tensor, it can be used iterative algorithm such as ALS, HALS or HOOI, commonly using HOSVD initialization, minimizing the cost function given in equation 4 [? ].

### 2.1.2. Non-negative Tucker Decomposition (NTD)

The NTD is a decomposition based on the Tucker model. It is a tensor factorization method with non-negativity constraints [1]. For the third-order case, the NTD, as defined by Cichocky [15], can be formulated as follows. Given a third-order tensor  $\mathcal{X} \in \mathbb{R}_+^{I_1 \times I_2 \times I_3}$  find a core tensor  $\mathcal{G} \in \mathbb{R}_+^{J_1 \times J_2 \times J_3}$  and the factor matrices  $\mathbf{U}^{(1)} \in \mathbb{R}_+^{I_1 \times J_1}$ ,  $\mathbf{U}^{(2)} \in \mathbb{R}_+^{I_2 \times J_2}$  and  $\mathbf{U}^{(3)} \in \mathbb{R}_+^{I_3 \times J_3}$  which performs the approximation given in Eq. (1), minimizing the cost function given in equation 4 by an iterative algorithm.

### 2.1.3. Integer Approximation Non-negative Tucker Decomposition (IANTD)

With the aim of preserving the original format of the HSI raw data, we propose an integer approximation of the NTD, which can be formulated as follows. Given a third-order non-negative

integer tensor  $\mathcal{X} \in \mathbb{N}^{I_1 \times I_2 \times I_3}$  find a core tensor  $\mathcal{G} \in \mathbb{N}^{I_1 \times I_2 \times I_3}$  and the factor matrices  $\mathbf{U}^{(1)} \in \mathbb{R}_+^{I_1 \times J_1}$ ,  $\mathbf{U}^{(2)} \in \mathbb{R}_+^{I_2 \times J_2}$  and  $\mathbf{U}^{(3)} \in \mathbb{R}_+^{I_3 \times J_3}$ , minimizing the cost function given in equation 4 through an iterative process. Each iteration, the values in the core tensor follow the integer restriction by an quantization function, while the projection matrix have no integer restriction so that they have a slight freedom to find better factorizations. The HOOI algorithm, described in [], has been used for the Tucker-based decompositions performed in this work.

### 3. Methodology

#### 3.1. Problem Statement

Let  $\mathcal{X} \in \mathbb{N}^{I_1 \times I_2 \times I_3}$  be a spectral image represented as a third-order tensor, and  $\mathbf{Y} \in \mathbb{N}^{I_1 \times I_2}$  its corresponding ground truth for  $C$  specific classes of interest. Using a Tucker-based decomposition, find a tensor  $\mathcal{G} \in \mathbb{R}^{I_1 \times I_2 \times I_3}$  highly representative of the raw data, and reduce the spectral dimensionality by selecting the  $B$  tensor bands with highest entropies to reduce computational complexity of pixel-wise classification CNNs, denoted as  $\Theta$  and with output  $\hat{\mathbf{Y}}$ , while preserving high performance.

#### 3.2. Mathematical Definition

The problem statement described above can be mathematically defined as the following optimization problem

$$\begin{aligned} \min_{\hat{\mathbf{Y}}} \quad & ||\mathbf{Y} - \hat{\mathbf{Y}}||_F^2 = \min_{\hat{\mathcal{G}}} ||\mathbf{Y} - \Theta(\hat{\mathcal{G}})||_F^2 \\ \text{subject to} \quad & \hat{\mathcal{G}} \in \mathbb{N}^{I_1 \times I_2 \times B} \subset \mathcal{G} \quad \text{subtensor of the core tensor, and} \\ & B = \min(b) |H(G_b) > T \max(\mathbf{h})| \quad \text{number of selected bands.} \end{aligned} \quad (5)$$

and the Tucker-based decomposition is mathematically defined as

$$\begin{aligned} \min_{\mathcal{G}, \mathbf{U}^{(1)}, \mathbf{U}^{(2)}, \mathbf{U}^{(3)}} \quad & ||\mathcal{X} - \mathcal{G} \times_1 \mathbf{U}^{(1)} \times_2 \mathbf{U}^{(2)} \times_3 \mathbf{U}^{(3)}||_F^2 \\ \text{subject to} \quad & \mathbf{U}^{(1)} = \mathbf{U}^{(2)} = \mathbf{I} \quad \text{Tucker-1 model} \\ & \mathbf{U}^{(3)} \in \mathbb{R}_+^{I_3 \times J_3} \quad \text{non-negative projection matrix,} \\ & \mathcal{G} \in \mathbb{N}^{I_1 \times I_2 \times J_3} \quad \text{non-negative and integer constraints,} \\ & J_n = I_n \quad \text{for } n = 1, 2, 3 \quad \text{no compression, and} \\ & \xi(\hat{\mathcal{X}}) \leq \xi_s \quad \text{measure of representativity.} \end{aligned} \quad (6)$$

The following subsections describe the big picture of the framework proposed in this work, which is summarized in three steps: tensor decomposition, band selection and classification.

#### 3.3. Spectral image decomposition

Given a spectral image  $\mathcal{X} \in \mathbb{N}^{I_1 \times I_2 \times I_3}$ , where  $I_1, I_2$  represents its spatial dimensionality,  $I_3$  the number of spectral bands, and  $\mathbb{N}$  the set of natural numbers, a 3rd-mode fiber  $\mathbf{x}_{i_1 i_2}$  represents the spectral signature of pixel  $i_1 i_2$  and can be represented by the Linear Mixing Model (LMM) as follows

$$\mathbf{x}_{i_1 i_2} = \alpha_{i_1 i_2} \mathbf{M} + \eta_{i_1 i_2} \quad (7)$$

where  $\alpha_{i_1 i_2}$  represents the abundance vector at pixel  $i_1 i_2$ ,  $\mathbf{M}$  denotes the endmember matrix, and  $\eta_{i_1 i_2}$  represents an additive noise vector. The abundance vectors  $\alpha_{i_1 i_2}$  must always satisfy two constraints, i) the non-negativity,  $\alpha_{i_1 i_2 c} \geq 0$  for all  $c = 1, \dots, C$ , and ii) the sum-to-one restriction,  $\sum_{c=1}^C \alpha_{i_1 i_2 c} = 1$ .

In order to achieve raw data dimensionality reduction, while preserving neighboring pixel correlation and leading spectral signatures into tensor signatures, a restricted version of the TKD,



known as the Tucker-1 model, is developed, where the projection matrices  $\mathbf{U}^{(1)}$  and  $\mathbf{U}^{(2)}$  are substituted in 1 by the identity matrix  $\mathbf{I}$ , i.e.,

$$\mathbf{X} = \mathbf{G} \times_1 \mathbf{I} \times_2 \mathbf{I} \times_3 \mathbf{U} + \mathbf{E} = \mathbf{G} \times_3 \mathbf{U} + \mathbf{E} \quad (8)$$

The core tensor can be computed by

$$\mathbf{G} = \mathbf{X} \times_3 \mathbf{U}^+ \quad (9)$$

where  $\mathbf{U}^+$  denotes the pseudoinverse matrix. If  $\mathbf{U}^+ = \mathbf{V}$ , each element of  $\mathbf{G}$  is computed as

$$g_{i_1 i_2 j_3} = \sum_{i_3=1}^{I_3} x_{i_1 i_2 i_3} v_{i_3 j_3} = \mathbf{x}_{i_1 i_2:} \mathbf{V}_{:j_3} \quad (10)$$

Thus, the 3rd-mode fibers of a core tensor at position  $i_1, i_2$  can be computed by

$$\mathbf{g}_{i_1 i_2:} = \mathbf{x}_{i_1 i_2:} \mathbf{V} \quad (11)$$

and from Eq. 7 and 11

$$\mathbf{g}_{i_1 i_2:} = (\boldsymbol{\alpha}_{i_1 i_2:} \mathbf{M} + \boldsymbol{\eta}_{i_1 i_2:}) \mathbf{V} \quad (12)$$

$$\mathbf{g}_{i_1 i_2:} = \boldsymbol{\alpha}_{i_1 i_2:} \mathbf{M} \mathbf{V} + \boldsymbol{\eta}_{i_1 i_2:} \mathbf{V} \quad (13)$$

Hence, doing  $\mathbf{M} \mathbf{V} = \mathbf{S}$ , the equivalent endmember matrix in the new tensor bands domain, and  $\boldsymbol{\eta}_{i_1 i_2:} \mathbf{V} = \boldsymbol{\gamma}_{i_1 i_2:}$ , the additive noise vector, each fiber of the core tensor, i.e.,  $\mathbf{g}_{i_1 i_2:}$ , takes a new representation in the tensor bands domain and can be similarly defined as the LMM in 7

$$\mathbf{g}_{i_1 i_2:} = \boldsymbol{\alpha}_{i_1 i_2:} \mathbf{S} + \boldsymbol{\gamma}_{i_1 i_2:} \quad (14)$$

By the properties of the TKD, these new tensor signatures are regarded to ease the between classes discrimination in lower data dimensionality, since the first tensor bands generally contain the larger eigenvectors of the decomposition. The following section describes the tensor bands selection process.

### 3.4. Dimensionality reduction

Under the principle of PCA [], the eigenvectors associated with larger eigenvalues are considered to keep more intrinsic information of the raw data []. Considering that each band of the core tensor is an image, just in a different domain than the original tensor dataset, it is possible to quantify the uncertainty, to estimate the information, by the Shannon entropy  $H$  computed as

$$H(G) = - \sum_{g \in \Omega} p(g) \log p(g) \quad (15)$$

for the discrete random variable  $G$ , regarded to be a tensor band, with probability space  $(\Omega, \Sigma, p(g))$ , where  $\Omega = \{0, 1, 2, \dots, 2^n\}$ ,  $n$  denotes the number of bits needed to store the maximum value of  $G$ ,  $\Sigma = \{\sigma_1, \sigma_2, \dots\}$  and  $\sigma_n \subset \Omega$ , and probability mass function  $p(g) = \Pr\{G = g\}$ .

Let  $\mathbf{h}$  be a vector of the entropies of each tensor band sorted in decreasing order, the number of tensor bands selected  $B$  to be the input of the CNN is determined by

$$B = \min(b) | H(G_b) > T \max(\mathbf{h}) \quad (16)$$

where  $G_b$  represents the tensor band  $b$  as random variable, for  $b = 1, \dots, J_3$ , and  $T$  denotes a given threshold value. According to PCA theory, the eigenvectors corresponding to the front elements of the core tensor  $\mathbf{G}$  preserve the most intrinsic information of the original dataset, which may be quantified

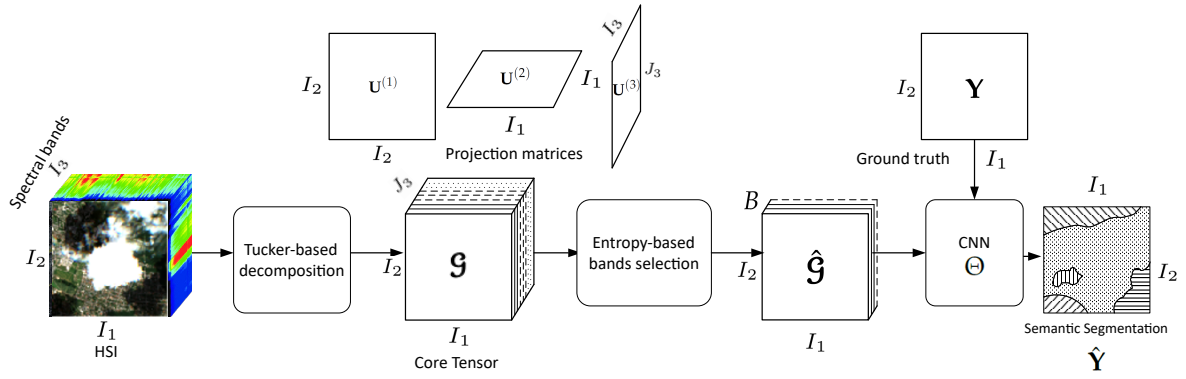


**Figure 2.** Big picture of the framework proposed.

by the Shannons entropy. From Eq. 16, the number of selected bands depends on the entrop of the given tensor. The smaller the value of  $T$  is, the larger the number of selected bands is and, in turn, the more detailed features inputs the CNN.

### 3.5. Pixel-wise classification CNN

Let  $\hat{\mathbf{G}} \in \mathbb{R}^{I_1 \times I_2 \times B}$  be the lower dimensionality core tensor, with  $B$  selected bands, and  $\mathbf{Y} \in \mathbb{C}^{I_1 \times I_2}$  its corresponding ground truth, where  $\mathbb{C}$  denotes the set of  $C$  different classes.  $\hat{\mathbf{G}}$  and  $\mathbf{Y}$  form the input tuple to the CNN classifier denoted as  $\Theta$ , which produce a prediction matrix  $\hat{\mathbf{Y}} \in \mathbb{C}^{I_1 \times I_2}$ , i.e.,

$$(\hat{\mathbf{G}}, \mathbf{Y}) \xrightarrow{\Theta} \hat{\mathbf{Y}} \quad (17)$$

Generally, CNNs are composed by a set of convolutional, Rectified Linear Unit (ReLU) and pooling/unpooling layers. The ReLU activation function generates activation maps, which identify features of a specific class in the image. At last layer, the activation maps are introduced to a softmax function, which output a probability distribution tensor  $\mathcal{P}$  over  $C$  different classes. Let  $\mathbf{Z} \in \mathbb{R}^{I_1 \times I_2 \times C}$  be a tensor with the set of activation maps at last layer and  $\mathbf{z}$  a 3rd-mode fiber of  $\mathbf{Z}$ , then

$$\delta_k(\mathbf{z}) = \frac{e^{z_k}}{\sum_{c=1}^C e^{z_c}} \quad (18)$$

where  $\delta_k(\cdot)$  denotes the softmax function and  $k$  the element of the output vector. Each fiber  $\mathbf{p}_{i_1 i_2}$  is the predicted probability distribution at pixel  $i_1, i_2$ , which has a wide relation with the contribution parameter  $\alpha_{i_1 i_2}$  in the core tensor LMM (Eq. 14). The highest probability or contribution value indicates the truth or predicted class respectively. Figure 2 shows the big picture summarizing the framework proposed.

## 4. Experimental Results

The set of evaluation metrics used in this work can be divided in two groups, metrics of the algorithms used in the framework, and metrics to evaluate classification performance of the whole framework proposed. Additionally, we considered a divergence information metric to quantify the representativity level of the lower dimensionality tensor.

### 4.1. Relative Mean Square Error (RMSE)

RMSE is used in this work to measure the distance between the raw data  $\hat{\mathbf{x}}$  and the reconstructed tensor  $\hat{\mathbf{x}}$  produced by the Tucker-based decompositions considered in this work, and it is computed as

$$\zeta(\hat{\mathbf{x}}) = \frac{\|\hat{\mathbf{x}} - \mathbf{x}\|_F^2}{\|\mathbf{x}\|_F^2}, \quad (19)$$



where  $\xi(\cdot)$  denotes the reconstruction error.

#### 4.2. Loss function

The error for the current state of an ANN must be computed each epoch as part of the optimization algorithm. Loss functions can be used to estimate the difference between the labels  $\mathbf{Y}$  and its corresponding prediction  $\hat{\mathbf{Y}}$  of a model so that the weights are updated to reduce the error on the next evaluation. The Frobenius norm is one of the typically used functions to evaluate the loss of an ANN. For the particular case of image classification it can be written as

$$J(\hat{\mathbf{Y}}) = \sum_{i_1=1}^{I_1} \sum_{i_2=1}^{I_2} \|y_{i_1,i_2} - \hat{y}_{i_1,i_2}\|_F^2 \quad (20)$$

where  $J(\hat{\mathbf{Y}})$  denotes the loss of the classifier.

#### 4.3. Jensen-Shannon Divergence (JSD)

This information theory metric is used to quantify how representative the core tensor of a decomposition is from raw data. JSD is computed as

$$D_{JS}(\mathcal{X}||\mathcal{G}) = \frac{1}{2}D_{KL}(\mathcal{X}||\mathcal{M}) + \frac{1}{2}D_{KL}(\mathcal{G}||\mathcal{M}) \quad (21)$$

where  $D_{JS}(\mathcal{X}||\mathcal{G})$  represents the JSD of two probability distributions  $\mathcal{X}$  and  $\mathcal{G}$ ,  $\mathcal{M} = \frac{\mathcal{X}+\mathcal{G}}{2}$  is the mean of the two probability distributions, and  $D_{KL}(\cdot)$  denotes the Kullback-Leibler divergence, which is a asymmetric version of the JSD and it is computed as

$$D_{KL}(\mathcal{X}||\mathcal{G}) = \sum_{i=1}^I p(x_i) \log \frac{p(x_i)}{p(g_i)} \quad (22)$$

where  $p(x_i)$  and  $g(x_i)$  represent the probability of the  $i$ -th element at distributions  $\mathcal{X}$  and  $\mathcal{G}$  respectively.

On the other hand, the datasets used for experiments in this work are considerably imbalanced. For this reason, we selected the metrics based on the works of Luque et al. [], Chicco et al. [] and Grandini et al. [], where they assess the impact of the imbalance and propose a set of metrics with lower bias in function of the imbalance and depending on the confusion matrix.

In order to fair evaluate performance of the classifier and to compare our work with others of the state of the art, we selected four main performance evaluation metrics. Pixel Accuracy (PA) is used to compute a ratio between the amount of correctly classified pixels and the total number of pixels. Despite this metric is highly biased for multiclass imbalanced dataset, it is one of the most popularly used in the state-of-art. Given a confusion matrix  $\mathbf{M} \in \mathbb{N}^{C \times C}$  relating the True Positive (TP), True Negatives (TN), False Positives (FP) and False Negatives (FN), PA is computed by Eq. 23. Cohen's Kappa coefficient and Matthews Correlation Coefficient (MCC) are alternative measures less affected by the unbalance issue [? ]. Kappa and MCC are computed by 24 and 25 respectively. Last, F1 score is employed as complementary metric to further weight the percentage of TP, since F1 is independent from TN (See Eq. ??).

#### 4.4. CNN Specifications

The model used to evaluate the framework proposed in this work is Segnet []. Table 4 shows the hyperparameters of the CNN set by cross-validation and the hardware specifications.

#### 4.5. Cases study

For this work, one multispectral dataset and three popular hyperspectral dataset were selected. For a fair comparison with methodologies cited in Section 1.1, the dataset was processed with the

**Table 3.** Table of metrics used to evaluate CNN classification performance.

Metric	Formula
Pixel Accuracy	$PA = \frac{TP + TN}{TP + TN + FP + FN} \quad (23)$
Cohen's Kappa Coefficient	$\kappa = \frac{\rho_o - \rho_e}{1 - \rho_e} \quad (24)$
Matthews Correlation Coefficient	$MCC = \frac{TP \cdot TN - FP \cdot FN}{\sqrt{(TP + FP)(TP + FN)(TN + FP)(TN + FN)}} \quad (25)$

**Table 4.** Experiments' software and hardware specifications.

Hyperparameters	Software/Hardware
learning rate: $1 \times 10^{-3}$ epochs: 100 optimizer: Adam [] initialization: Xavier [] kernel dimensions: $3 \times 3$ Activation Function: ReLU / Softmax	Platform: Python 3.7 AI Framework: Tensorflow 1.13 GPU: NVIDIA GeForce GTX 1050 Ti Processor: Intel core i7 RAM: 8GB SSD: 128GB / HDD: 1TB

original information from the European Space Agency Sentinel-2 database and from the [Hyperspectral Remote Sensing Scenes](#) web page.

Table 5 summarizes the datasets used in this work, as well as their spatial and spectral characteristics, the number of classes and samples.

**Table 5.** Summary of the different dataset used for experiments in this work.

Dataset	Spatial dimensions	Bands	Classes	Samples
Sentinel-2 CNNMSI	$128 \times 128$	9	5	1,802,240
Indian Pines	$145 \times 145$	220	16	10,249
Salinas	$512 \times 217$	224	16	53,785
Pavia University	$610 \times 340$	103	9	40,076

#### 4.5.1. Case A: Sentinel-2 dataset

This dataset proposed by Lopez et al. [?] is composed of 110 RS Sentinel-2 scenarios from central Europe. It has 100 scenarios as the training space and 10 scenarios for testing, all of them with  $128 \times 128$  pixels with spatial resolution of  $20m^2$  and 9 spectral bands in the range  $490 - 2190nm$ . The labels are semi-manually assigned for five classes of interest: vegetation, soil, water, clouds and shadows. Data are available in the link [Sentinel-2 Dataset](#).

Sentinel-2 images, in this dataset, are in Level-2A ESA product type, which provides images in top-of-atmosphere reflectance integer units. This ease the dataset normalization dividing it by 10000 to obtain reflectance values in 0 to 1 range []. Another important consideration is the dataset imbalance analysis, which can be seen in Table 6. Vegetation and soil are the classes with higher positive imbalance encompassing 48.92% and 23.35% of the samples respectively. On the other hand, shadow class has only 2.5% of the whole dataset. Comparing with vegetation and soil, there is a significant imbalance among them. For this reason, the performance evaluation metrics used in this work have been selected considering this class imbalance.

This dataset can be characterized by information theory metrics. Figure 5 show the entropy level of the raw data spectral bands, where it can be seen that each band has high entropy. On the contrary, tensor bands generated in the Tucker-based decompositions generally carry the highest entropy to

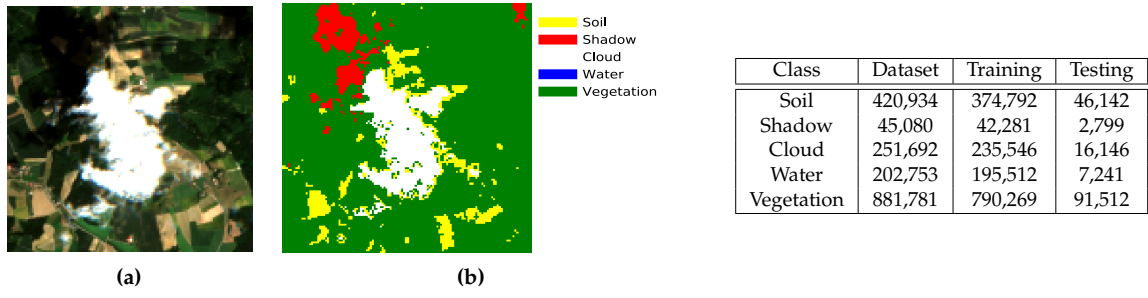


**Figure 4 & Table 5.** Sentinel-2 dataset a) True color image and b) Ground truth. Table) Samples per class.

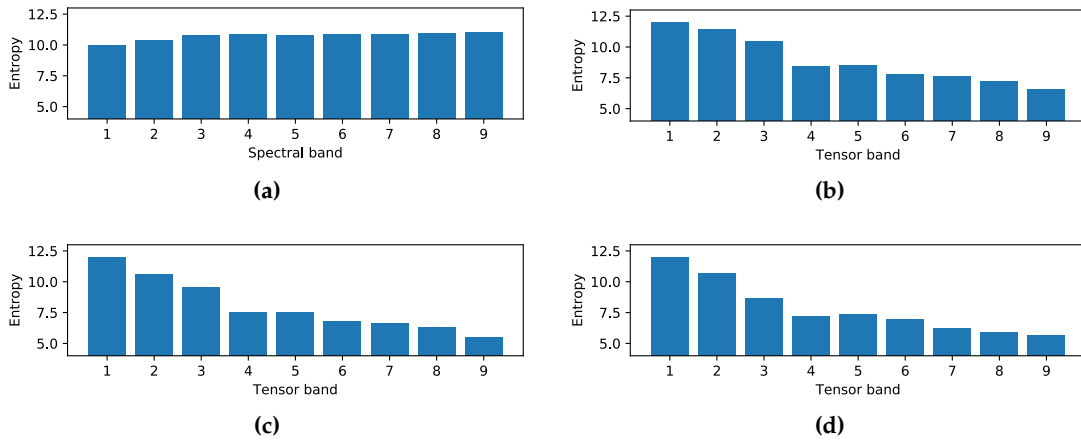


**Figure 5.** Sentinel-2 dataset entropy, a) raw data, and b) TKD, c) NTD and d) IANTD core tensors.

the frontal bands and have a decreasing behavior. Other works also use mutual information between bands, to discredit those bands with high redundancy.

The five classes of interest in this dataset show spectral signatures easy to discern, since their reflectance are considerably distanced one from the others in more than three wavelengths, as can be seen in Figure 6. When a Tucker-based decomposition is applied to the raw data, these signatures behaves differently. It is worth noting that, the signatures in the new tensor band domain are easy diferenciabile in the first frontal bands, but they are highly correlated after the third one.

The low spectral dimensionality of Sentinel-2 dataset makes simpler the analysis of the distance metrics used in this work. Figure 7 shows the reconstruction error comparing the three decompositions used in this work for variable number of 3rd-mode tensor dimensionality. As it can be expected, the larger the number of bands retained, the lower the reconstruction error. Also, non-negative and integer restricted decompositions produce slower error decrease than the no constrained TKD.

On the other hand, Figure 8 shows that compressed tensors with lower number of tensor bands selected, with respect to the raw data, have higher level of representativity than those with higher dimensionality. In this case, TKD cores look less representative due to negative values, which diverge widely from the positive ones in the raw data. Nevertheless, under Lathauwer criteria for all orthogonality [31], TKD present a much higher orthogonality, which is totally related to the freedom of the decomposition to find solutions in a wider domain. Figure 9 shows the norm criterion, which is generally satisfied in the three core tensors. However, as it can be anticipated, NTD and IANTD do not fulfilled the inner product criterion, and in turn, projection matrices are low orthogonal.

In terms of complexity, the execution time may be a metric to quantify the complexity reduction degree. Figure 10 shows that, as the number of tensor bands selected increases, the execution time rises exponentially.

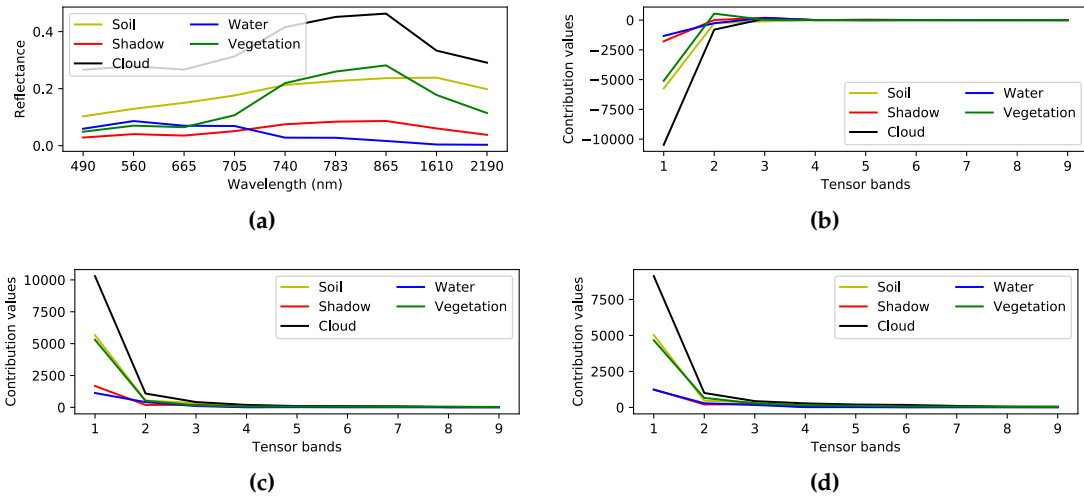


**Figure 6.** Spectral and tensor signatures of the five classes of interest in the a) original spectral bands, b) TKD core tensor bands, c) NTD core tensor bands and d) IANTD core tensor bands.

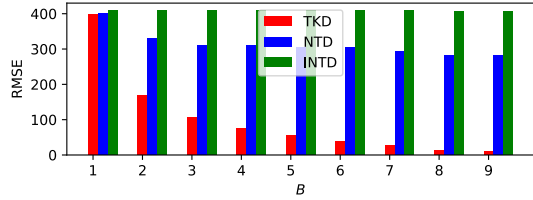


**Figure 7.** Reconstruction error for variable number of tensor bands.

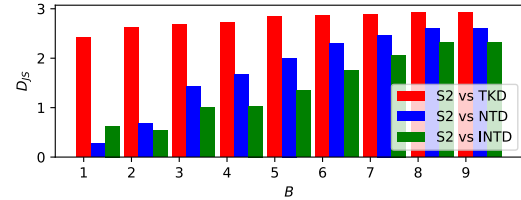


**Figure 8.** JSD between core tensor and raw data.

Finally, Figure 11 shows the PA for the three decomposition varying the number of selected bands. As point of comparison, dotted lines indicates the PA with the raw data as input to the CNN. TKD and IANTD are highly competitive with less than 25% of the original tensor dimensionality, while NTD proves to get better results, even than the raw data, with only 1 tensor band. This can also be seen in Table 6, where it is summarized the performance evaluation under the three metrics selected.

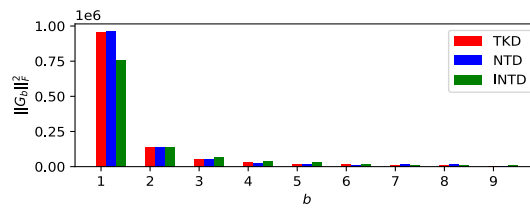


**Figure 9.** Tensor band Frobenius norm.

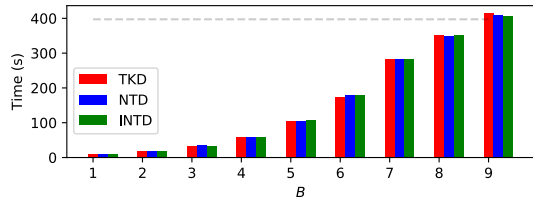


**Figure 10.** Execution time for variable compressed tensor dimensionality.

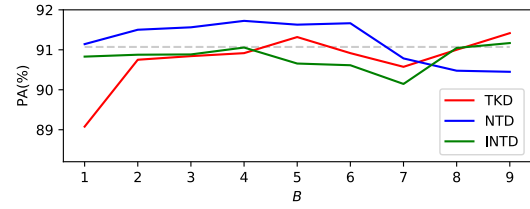


**Figure 11.** PA for variable number of selected bands.

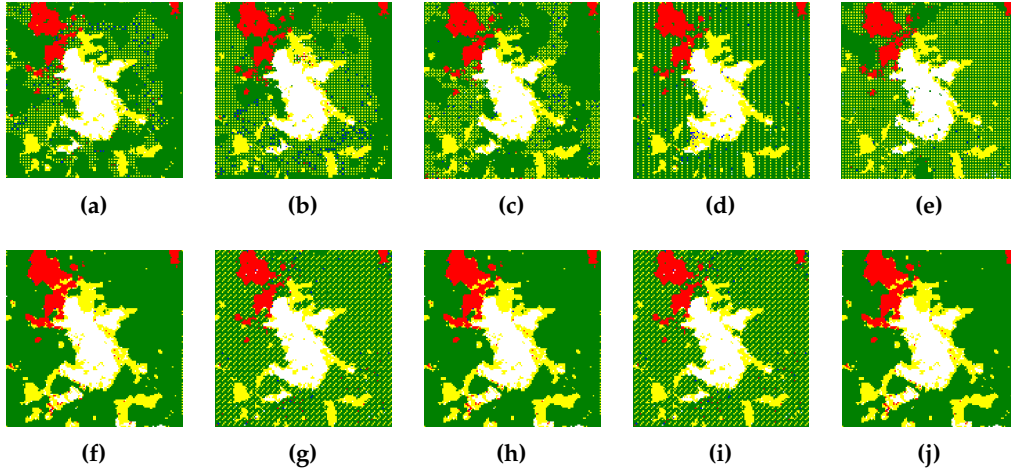


**Figure 12.** Qualitative results. Visualization of the predicted matrix of a testing scene with abundant vegetation and clouds, and presence of shadows and soil. Prediction after 100 epochs in the CNN used for this work a) with the original dataset without data compression, b) with TKD compressing to  $B = 5$ , c) with NTD and no compression,  $B = 9$ , d) with NTD to  $J_3 = 5$ , e) with NTD and no compression,  $B = 9$ , f) with INTD compressing to  $B = 5$  and g) with INTD and no compression,  $B = 9$ .

**Table 6.** Quantitative results<sup>1</sup> for the Sentinel-2 test dataset running in a NVIDIA GeForce GTX 1050 Ti GPU, Intel core i7 processor, 8 Gb RAM, SSD 128 Gb, and HDD 1 Tb. Decomposition reconstruction error, average processing time per scenario, PA and Kappa's coefficient results for  $J_3 = 1, \dots, 9$ .

$J_3$	TKD			NTD			INTD		
	PA	$\kappa$	MCC	PA	$\kappa$	MCC	PA	$\kappa$	MCC
1	0.9069	0.8466	0.8481	0.9076	0.8493	0.8511	0.9002	0.8355	0.8365
2	0.9005	0.8364	0.8376	0.9155	0.8610	0.8626	0.9043	0.8424	0.8439
3	0.9056	0.8446	0.8454	0.8734	0.7956	0.8010	0.8999	0.8366	0.8384
4	0.8822	0.8081	0.8113	0.8675	0.7863	0.7926	0.8615	0.7776	0.7844
5	0.8968	0.8326	0.8346	0.8228	0.7222	0.7409	0.8703	0.7905	0.7956
6	0.8635	0.7805	0.7857	0.8637	0.7814	0.7875	0.8821	0.8084	0.8122
7	0.8973	0.8332	0.8357	0.8699	0.7905	0.7964	0.8635	0.7782	0.7820
8	0.8795	0.8061	0.8122	0.8544	0.7647	0.7709	0.9088	0.8503	0.8512
9	0.8696	0.7908	0.7983	0.9197	0.8675	0.8680	0.9057	0.8450	0.8461

<sup>1</sup> Raw data: PA = 0.8578,  $\kappa$  = 0.7709 and MCC = 0.7768.

#### 4.5.2. Case B: Indian Pines

This dataset is a scene produced by AVIRIS in North-western Indiana and consists of  $145 \times 145$  pixels and 224 spectral bands in the wavelength range  $0.4 - 2.5 \mu m$ . The Indian Pines scene contains two-thirds agriculture, and one-third forest or other natural perennial vegetation. There are two major dual lane highways, a rail line, as well as some low density housing, other built structures, and smaller

roads. Since the scene is taken in June some of the crops present, corn, soybeans, are in early stages of growth with less than 5% coverage. The ground truth available is designated into sixteen classes and is not all mutually exclusive. Indian Pines data are available at [Indian Pines dataset](#). Figure 13a shows the true color, Figure 13b the ground truth and Table 4 shows the number of samples for each class.

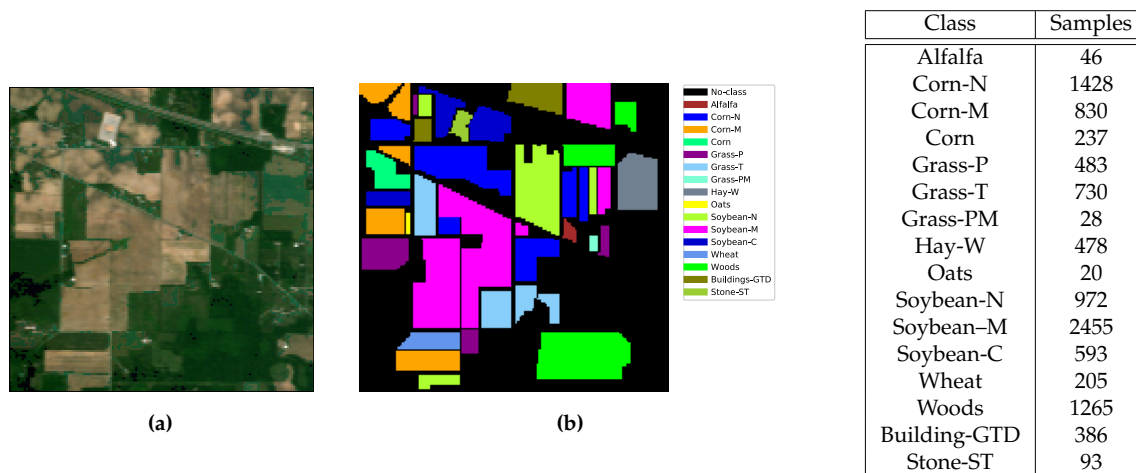


**Figure 13 & Table 7.** Indian Pines dataset, a) True color image and b) Ground truth. Table) Samples per class

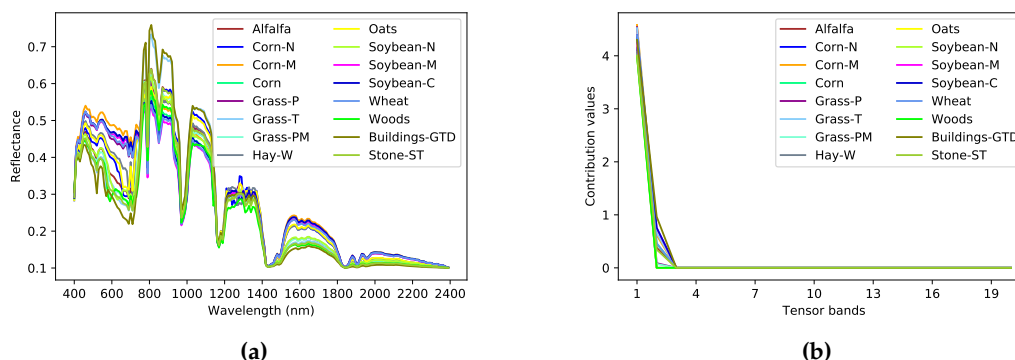


**Figure 14.** Behavior of the 16 classes of the Indian Pines dataset, a) in the spectral domain (spectral signatures) and b) in the the tensor bands domain after IANTD.



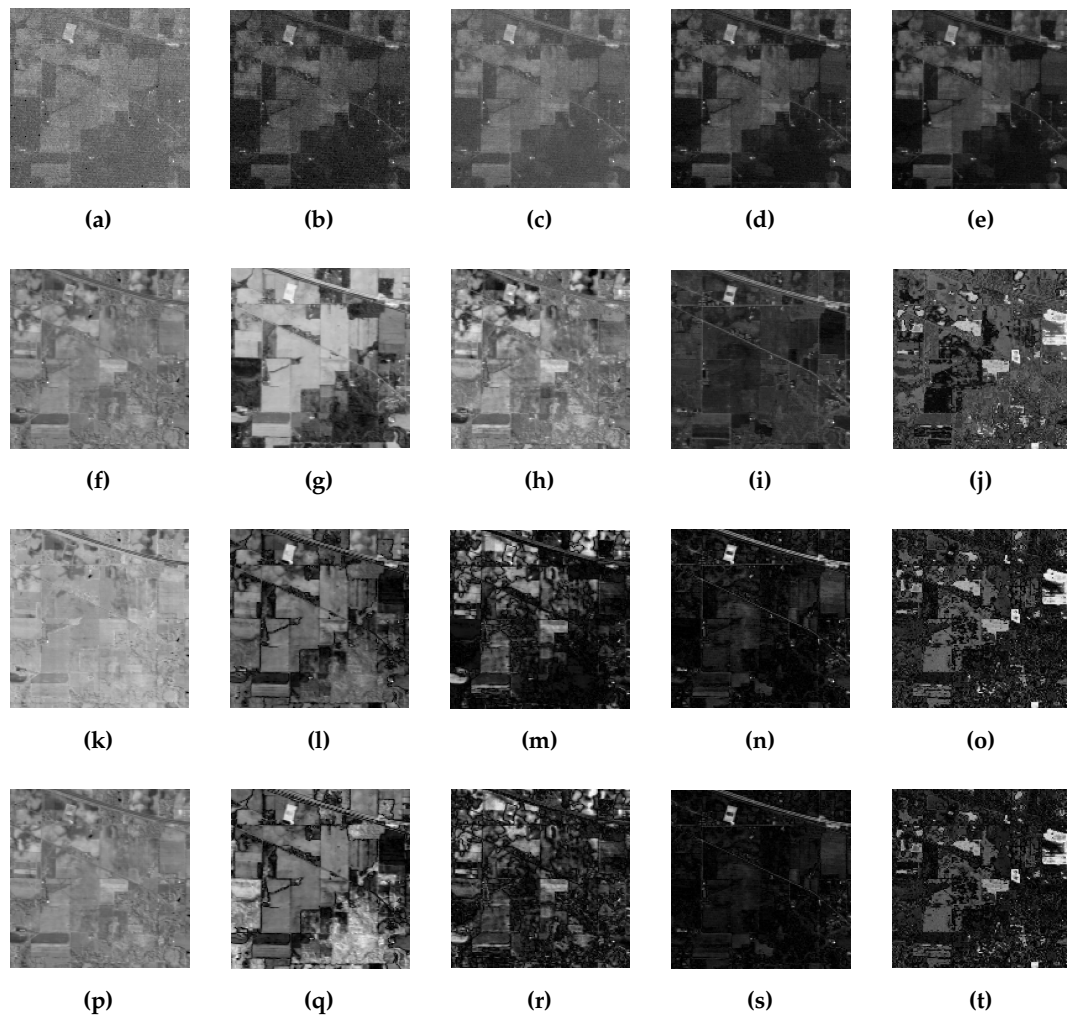


**Figure 15.** Visualisation of Indian Pines 1st to 5th 15a to 15e original spectral bands, 15f to 15j tensor bands with TKD, 15k to 15o tensor bands with NTD, and 15p to 15t tensor bands with INTD.

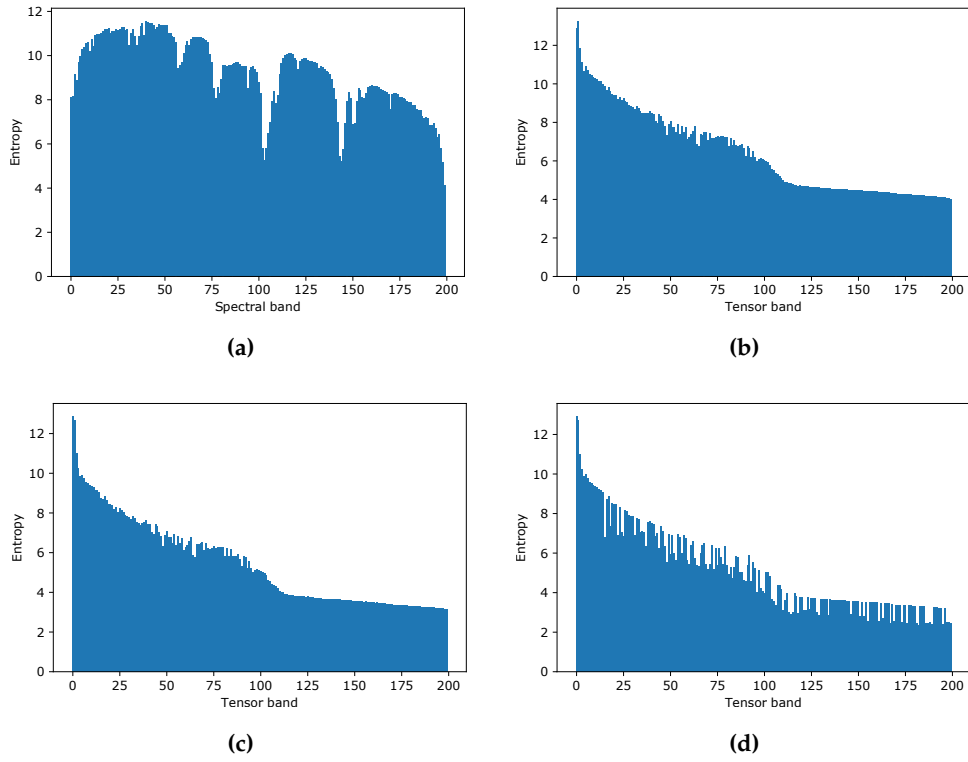


**Figure 16.** Indian Pines entropy of each band in the a) original dataset, and b) TKD, c) NTD and d) INTD core tensors.

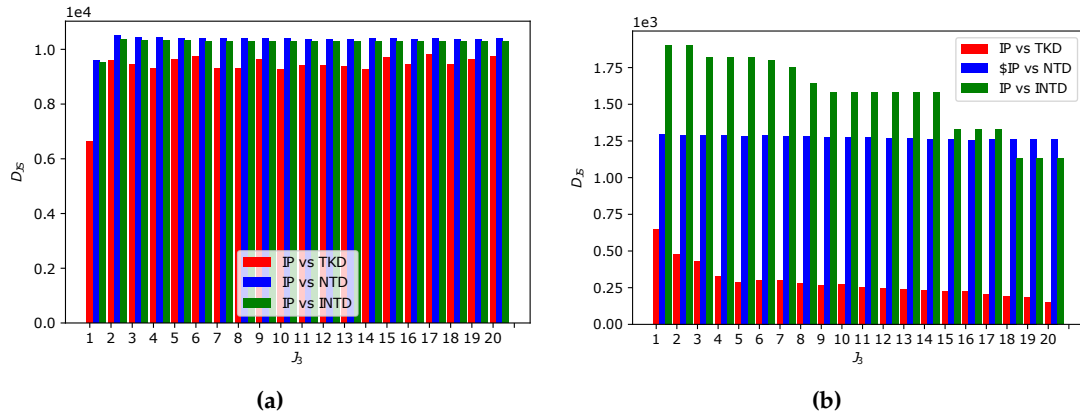


**Figure 17.** JSD between a) TKD / NTD / INTD core tensor vs input dataset, and b) TKD / NTD / INTD reconstruction vs input dataset.

As shown by the results obtained by measuring the divergence between the original dataset and its reconstruction for each decomposition model, non-negative decompositions produce a reconstruction error greater than the TKD, see Table ?? . Furthermore, the fall of the error is very slow as the 3-rank of the decomposition increases.

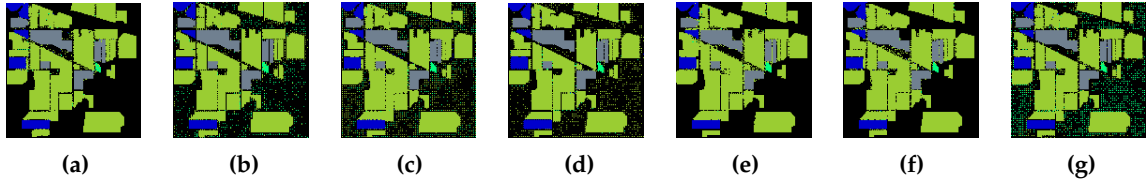


**Figure 18.** Qualitative results. Visualization of the predicted matrix of the Indian Pines dataset. Prediction after 100 epochs in the CNN used for this work a) with the original dataset without data compression, b) with TKD compressing to  $J_3 = 5$ , c) with NTD and no compression,  $J_3 = 9$ , d) with NTD to  $J_3 = 5$ , e) with NTD and no compression,  $J_3 = 9$ , f) with INTD compressing to  $J_3 = 5$  and g) with INTD and no compression,  $J_3 = 9$ .

**Table 8.** Quantitative results<sup>1</sup> for the Indian Pines dataset running in a NVIDIA GeForce GTX 1050 Ti GPU! (GPU!), Intel core i7 processor, 8 Gb RAM, SSD 128 Gb, and HDD 1 Tb. Decomposition reconstruction error, average processing time per scenario, PA and Kappa's coefficient results for  $J_3 = 1, \dots, 10$ .

$J_3$	TKD				NTD				INTD			
	$\zeta$	Time (s)	PA (%)	$\kappa$	$\zeta$	Time (s)	PA (%)	$\kappa$	$\zeta$	Time (s)	PA (%)	$\kappa$
1	375.365	15.83	82.93	0.8207	375.36	16.21	86.41	0.8252	2965.49	15.72	86.75	0.7799
2	140.6	32.83	92.51	0.9020	67.53	31.55	92.87	0.8844	2965.49	39.63	91.82	0.8972
3	116.63	56.56	88.03	0.8946	343.33	57.32	92.31	0.9074	2957.91	62.31	93.25	0.8427
4	105.57	92.13	91.76	0.8766	343.43	97.10	90.83	0.8534	2951.48	98.94	88.39	0.8855
5	98.85	156.21	88.53	0.8981	343.33	151.23	92.75	0.8597	2938.82	164.32	89.91	0.8478
6	92.52	298.80	83.99	0.8653	339.64	301.09	89.90	0.8990	2929.61	313.21	92.36	0.7913
7	87.41	520.13	89.21	0.8973	337.89	515.63	92.74	0.8523	2895.02	535.08	88.94	0.8540
8	79.53	715.69	88.33	0.8561	335.90	704.21	89.86	0.8599	2876.32	732.12	92.15	0.8469
9	76.15	881.21	89.97	0.8853	335.91	876.36	92.03	0.8891	2866.45	901.35	92.01	0.8603
10	72.67	934.78	88.61	0.8871	335.74	910.84	92.93	0.8864	2854.12	978.54	91.95	0.8462

<sup>1</sup> For the original Indian Pines dataset: Time = 878.09 s, PA = 91..22%,  $\kappa$  = 0.9040.

## 5. Discussion and Comparison

In this work, the hyperspectral input dataset is decomposed by a Tucker-based decomposition model to transform them from the spectral bands domain (wavelength) to a new tensor bands domain. The decompositions are restricted to preserve the spatial domain and to compress the spectral domain. Figure 14 it can be seen how the endmembers of the materials of interest behave in a way that, from a salient band point of view, the first new tensor bands are able to provide enough information to a CNN to differentiate diverse materials. On the other hand, From the information theory point of view, the entropy computed for each original and core tensors band reinforce this assertion (See Figure 16).

Unlike previous works, the introduction of information metrics in this work aids to trade off the empirical setting of the multirank TKD parameters. Although the process is still semi-empirical, it is based on metrics that quantify the amount of information and the divergence from the original data. It is worth noting that, in this work, the compression is developed only in the spectral domain, but the basis of the proposal can also be applicable for other kinds of decomposition.

Qualitative results (Figures 12–18) and quantitative results in Figure ?? present the performance evaluation of the CNN, based on PA, comparing the three models based on TKD. Comparing with results shown in previous works [? ], [? ], [? ], the proposed INTD overcomes unsupervised classification algorithms, as well as decomposition without non-negativity and integer restrictions. While it is true that the PA metric is not the best for an unbalanced dataset, it is a good starting point for a general comparison. Nevertheless, the kappa coefficients results, shown in Figure ??, show greater stability in classification for the TKD, but as the value of  $J_3$  increases, the NTD and INTD improve their performance, while the TKD fall. this can be attributed to the phenomenon of overfitting.

Tables 6 and 8 allow us to make a fair comparison among the Tucker-based decompositions. First of all, as expected, the TKD reconstruction error decrease faster than the approximation with

non-negativity and integer constraints. On the other hand, the analysis of PA and the Kappa's coefficient, in combination with the entropy, give a measure linked to the diminution of execution time in favor of the NTD and the proposed INTD approximation.

## 6. Conclusions

In this work, we had the purpose of improving the features of a multi- or hyperspectral image, while reducing dimensionality and, in turn, the computational complexity of a classification CNN. From the results presented above and the analysis of each metric, it has been shown that the constraints imposed to a decomposition model, as the NTD and INTD, produce an improvement in classification metrics of CNN. It is worth noting that, depending on the model of the classifier, the TD should be limited to provide characteristics that aids the classifier to improve its performance.

Results shown in Figure 17 we can conclude that the proposed integer non-negative approximation

### 6.1. Open issues

- 
- 
- 

**Author Contributions:** Conceptualization, J.L.; formal analysis, D.T.; investigation, J.L.; methodology, J.L., D.T., and C.A.; resources, C.A.; software, J.L.; supervision, D.T. and C.A.; validation, D.T. and C.A.; writing—original draft, J.L. and D.T.

**Funding:** This work was supported by the National Council of Science and Technology CONACYT of Mexico under grant XXXXXXXX.

**Conflicts of Interest:** The authors declare no conflict of interest.

## References

1. Tempfli, K.; Huurneman, G.; Bakker, W.; Janssen, L.; Feringa, W.; Gieske, A.; Grabmaier, K.; Hecker, C.; Horn, J.; Kerle, N.; et al. *Principles of Remote Sensing: An Introductory Textbook*, 4th ed.; ITC: Geneva, Switzerland, 2009.
2. He, Z.; Hu, J.; Wang, Y. Low-rank tensor learning for classification of hyperspectral image with limited labeled sample. *IEEE Signal Process.* **2017**, *145*, 12–25.
3. Richards, A.; Xiuping, J.J. Band selection in sentinel-2 satellite for agriculture applications. In *Remote Sensing Digital Image Analysis*, 4th ed.; Springer-Verlag: Berlin, Germany, 2006.
4. Zhang, T.; Su, J.; Liu, C.; Chen, W.; Liu, H.; Liu, G. Band selection in sentinel-2 satellite for agriculture applications. In Proceedings of the 23rd International Conference on Automation & Computing, University of Huddersfield, Huddersfield, UK, 7–8 September 2017.
5. Xie, Y.; Zhao, X.; Li, L.; Wang, H. Calculating NDVI for Landsat7-ETM data after atmospheric correction using 6S model: A case study in Zhangye city, China. In Proceedings of the 18th International Conference on Geoinformatics, Beijing, China, 18–20 June 2010.
6. Gao, B. NDWI—A normalized difference water index for remote sensing of vegetation liquid water from space. *Remote Sens. Environ.* **1996**, *58*, 1–6.
7. Ham, J.; Chen, Y.; Crawford, M.; Ghosh, J. Investigation of the random forest framework for classification of hyperspectral data. *IEEE Trans. Geosci. Remote Sens.* **2005**, *43*, 492–501.
8. Hearst, Marti A. Support Vector Machines. *IEEE Intell. Syst. J.* **1998**, *13*, 18–28.
9. Huang, X.; Zhang, L. An SVM Ensemble Approach Combining Spectral, Structural, and Semantic Features for the Classification of High-Resolution Remotely Sensed Imagery. *IEEE Trans. Geosci. Remote Sens.* **2013**, *51*, 257–272.
10. Delalieux, S.; Somers, B.; Haest, B.; Spanhove, T.; Vanden Borre, J.; Mucher, S. Heathland conservation status mapping through integration of hyperspectral mixture analysis and decision tree classifiers. *Remote Sens. Environ.* **2012**, *126*, 222–231.
11. Kemker, R.; Salvaggio, C.; Kanan, C. Algorithms for semantic segmentation of multispectral remote sensing imagery using deep learning. *ISPRS J. Photogramm. Remote Sens.* **2018**, *145*, 60–77.

12. Pirotti, F.; Sunar, F.; Piragnolo, M. Benchmark of machine learning methods for classification of a sentinel-2 image. In Proceedings of the XXIII ISPRS Congress, Prague, Czech Republic, 12–19 July 2016.
13. Mateo-García, G.; Gómez-Chova, L.; Camps-Valls, G. Convolutional neural networks for multispectral image cloud masking. In Proceedings of the IGARSS, Fort Worth, TX, USA, 23–28 July 2017.
14. Guo, X.; Huang, X.; Zhang, L.; Zhang, L.; Plaza, A.; Benediktsson, J. A. Support Tensor Machines for Classification of Hyperspectral Remote Sensing Imagery. *IEEE Trans. Geosci. Remote Sens.* **2016**, *54*, 3248–3264.
15. Cichocki, A.; Mandic, D.; De Lathauwer, L.; Zhou, G.; Zhao, Q.; Caiafa, C.; Phan, H. Tensor Decompositions for Signal Processing Applications: From two-way to multiway component analysis. *IEEE Signal Process. Mag.* **2015**, *32*, 145–163.
16. Jolliffe, I.T. *Principal Component Analysis*, 2nd ed.; Springer Verlag: New York, NY, USA, 2002.
17. Kolda, T.; Bader, B. Tensor Decompositions and Applications. *SIAM Rev.* **2009**, *51*, 455–500.
18. Lopez, J.; Santos, S.; Torres, D.; Atzberger, C. Convolutional Neural Networks for Semantic Segmentation of Multispectral Remote Sensing Images. In Proceedings of the LATINCOM, Guadalajara, Mexico, 14–16 November 2018.
19. European Space Agency. Available online: <https://sentinel.esa.int/web/sentinel/missions/sentinel-2> (accessed on 15 July 2019).
20. Kemker, R.; Kanan, C. Deep Neural Networks for Semantic Segmentation of Multispectral Remote Sensing Imagery. *arXiv* **2017**, arXiv:abs/1703.06452.
21. Hamida, A.; Benoît, A.; Lambert, P.; Klein, L.; Amar, C.; Audebert, N.; Lefèvre, S. Deep learning for semantic segmentation of remote sensing images with rich spectral content. In Proceedings of the IGARSS, Fort Worth, TX, USA, 23–28 July 2017.
22. Wang, Q.; Lin, J.; Yuan, Y. Salient Band Selection for Hyperspectral Image Classification via Manifold Ranking. *IEEE Trans. Neural Netw. Learn. Syst.* **2016**, *27*, 1279–1289.
23. Li, S.; Qiu, J.; Yang, X.; Liu, H.; Wan, D.; Zhu, Y. A novel approach to hyperspectral band selection based on spectral shape similarity analysis and fast branch and bound search. *Eng. Appl. Artif. Intell.* **2014**, *27*, 241–250.
24. Zhang, L.; Zhang, L.; Tao, D.; Huang, X.; Du, B. Compression of hyperspectral remote sensing images by tensor approach. *Neurocomputing* **2015**, *147*, 358–363.
25. Astrid, M.; Lee, Seung-Ik. CP-decomposition with Tensor Power Method for Convolutional Neural Networks compression. In Proceedings of the BigComp, Jeju, Korea, 13–16 February 2017.
26. Chien, J.; Bao, Y. Tensor-factorized neural networks. *IEEE Trans. Neural Networks Learn. Syst.* **2018**, *29*, 1998–2011.
27. An, J.; Lei, J.; Song, Y.; Zhang, X.; Guo, J. Tensor Based Multiscale Low Rank Decomposition for Hyperspectral Images Dimensionality Reductio. *Remote Sens.* **2019**, *11*, 1485.
28. Li, J.; Liu, Z. Multispectral Transforms Using Convolution Neural Networks for Remote Sensing Multispectral Image Compression. *Remote Sens.* **2019**, *11*, 759.
29. An, J.; Song, Y.; Guo, Y.; Ma, X.; Zhang, X. Tensor Discriminant Analysis via Compact Feature Representation for Hyperspectral Images Dimensionality Reduction. *Remote Sens.* **2019**, *11*, 1822.
30. Absil, P.-A.; Mahony, R.; Sepulchre, R. *Optimization Algorithms on Matrix Manifolds*, 1st ed.; Princeton University Press: Princeton, NJ, USA, 2007.
31. De Lathauwer, L.; De Moor, B.; Vandewalle, J. On the best rank-1 and rank-( $R_1, R_2, \dots, R_N$ ) approximation of higher-order tensors. *SIAM J. Matrix Anal. Appl.* **2000**, *21*, 1324–1342.
32. Goodfellow, I.; Bengio, Y.; Courville, A. *Deep Learning*, 1st ed.; MIT Press, 2016.
33. Sheehan, B. N.; Saad, Y. Higher Order Orthogonal Iteration of Tensors (HOOI) and its Relation to PCA and GLRAM. In Proceedings of the 7th SIAM International Conference on Data Mining, Minneapolis, MN, USA, 26–28 April 2007.
34. Badrinarayanan, V.; Kendall, A.; Cipolla, R. SegNet: A Deep Convolutional Encoder-Decoder Architecture for Image Segmentation. *IEEE Trans. Pattern Anal. Mach. Intell.* **2017**, *39*, 2481–2495.
35. De Lathauwer, L.; De Moor, B.; Vandewalle, J. A Multilinear Singular Value Decomposition. *SIAM J. Matrix Anal. Appl.* **2000**, *21*, 1253–1278.
36. Rodes, I.; Inglada, J.; Hagolle, O.; Dejou, J.; Dedieu, G. Sampling strategies for unsupervised classification of multitemporal high resolution optical images over very large areas. In Proceedings of the 2012 IEEE International Geoscience and Remote Sensing Symposium, Munich, Germany, 22–27 July 2012.

**Sample Availability:** Samples of the compounds ..... are available from the authors.

4 64 © 2021 by the authors. Submitted to *Remote Sens.* for possible open access publication  
4 65 under the terms and conditions of the Creative Commons Attribution (CC BY) license  
4 66 (<http://creativecommons.org/licenses/by/4.0/>).